Chemical Science

ROYAL SOCIETY OF CHEMISTRY

EDGE ARTICLE

View Article Online
View Journal

Cite this: DOI: 10.1039/d6sc02303g

All publication charges for this article have been paid for by the Royal Society of Chemistry

Methyl-induced ring-locking strategy for concentration-independent MR-TADF emitters toward high-performance OLEDs with BT.2020 blue gamut

Gaoyu Li,†[a] Yuyuan Wang,†[a] Bo Wu,[b] Jinkun Bian,[a] Haozhi Xie,[a] Zhiwei Ma,[a] Hui Dai,[a] Zhan Yang,*[b] Xiangyu Ge*[c] and Zhenguo Chi *[ab]

Realizing deep-blue multi-resonance thermally activated delayed fluorescence (MR-TADF) emitters that simultaneously offer high efficiency and resistance to aggregation-caused quenching (ACQ) remains formidably challenging, severely limiting their practical application in BT.2020-compliant OLEDs. Herein, we report a series of high-performance deep-blue MR-TADF emitters with outstanding anti-ACQ characteristics *via* strategic peripheral methylation. By systematically varying the quantity and regiochemistry of methyl substituents on a **DABNA-NP** scaffold, we establish a comprehensive structure–property-performance relationship governing molecular rigidity and nonradiative decay processes. Photophysical and theoretical calculation analyses reveal that di-*ortho*-methyl substitution induces an effective "ring-locking" effect, significantly restricting peripheral phenyl rotations and low-frequency vibrations, thereby suppressing nonradiative relaxation without perturbing frontier molecular orbitals. Consequently, the three emitters (**2M-BN**, **3M-BN**, and **4M-BN**) realize narrow deep-blue emission with high PLQYs of 95–99% in 1 wt% doped films. Notably, all emitters display excellent resistance to ACQ, maintaining stable emission profiles over a wide doping range (1–15 wt%). OLEDs based on **2M-BN** consistently achieve high external quantum efficiencies of 23.3–26.9% while fully satisfying the BT.2020 blue standard (Commission Internationale de l' Éclairage *y* coordinate, CIE_y = 0.040–0.046). This work demonstrates a clear mechanistic link between steric methylation and vibrational confinement, providing a general molecular design principle for concentration-independent deep-blue MR-TADF emitters.

Received 20th March 2026
Accepted 8th May 2026

DOI: 10.1039/d6sc02303g

rsc.li/chemical-science

Introduction

Organic light-emitting diodes (OLEDs) have emerged as the mainstream technology for next-generation ultra-high-definition displays (*e.g.*, 4 K/8 K) due to their intrinsic advantages, including high contrast, rapid response times, and wide color gamuts.[1–3] Within OLED display technology, the development of deep-blue emitters that adhere to the Broadcast Television 2020 (BT.2020) standard is pivotal for expanding the color gamut and enhancing display quality.[4,5] The BT.2020 blue coordinates (Commission Internationale de l' Éclairage *y* coordinate, CIE_y < 0.046) demand exceptional color purity, which requires emitters to exhibit an extremely narrow emission spectrum to achieve the desired electroluminescence (EL) coordinates on the chromaticity diagram. Moreover, to meet the low power consumption requirements of commercial applications, these materials must also guarantee near-unity internal quantum efficiency (IQE). However, designing deep-blue emitters that simultaneously deliver ultra-high color purity (characterized by an ultra-narrow full width at half maximum, FWHM) and high efficiency remains a formidable challenge, rendering such materials exceedingly scarce in the OLED field. Although heavy-metal-based phosphorescent materials can harness 100% IQE owing to the possession of strong spin–orbit coupling (SOC),[6] with a few reports demonstrating efficient emission near the BT.2020 blue coordinates,[7–9] their progress is hindered by the high cost and scarcity of noble metals, along with limited structural diversity in the deep-blue regime. Consequently, there is an urgent need to develop novel deep-

[a]*Guangdong Engineering Technology Research Center for High-performance Organic and Polymer Photoelectric Functional Films State Key Laboratory of Optoelectronic Material and Technologies, School of Chemistry Sun Yat-sen University, Guangzhou 510275, China. E-mail: chizhg@mail.sysu.edu.cn*

[b]*School of Environmental and Chemical Engineering Wuyi University, Jiangmen 529020, China. E-mail: yangzhan@wyu.edu.cn*

[c]*Key Laboratory of Guangdong Higher Education Institutions of Northeast Guangdong New Functional Materials, School of Chemistry and Environment, Jiaying University, Meizhou, 514015, Guangdong, P.R. China. E-mail: gexy28@mail.sysu.edu.cn*

† Gaoyu Li and Yuyuan Wang contributed equally to this work.

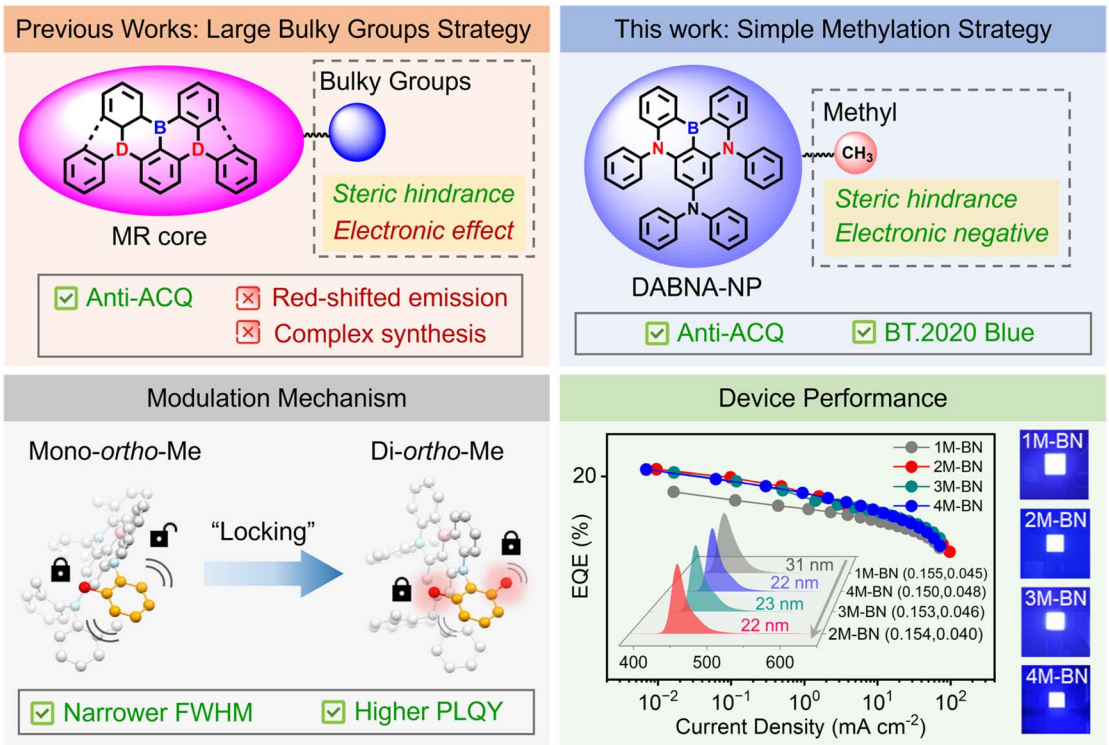

Fig. 1 The molecular design strategy in this work.

blue materials that offer ultra-high color purity, high efficiency, and cost-effectiveness.

Fortunately, multi-resonance thermally activated delayed fluorescence (MR-TADF) emitters, first proposed by Hatakeyama and co-workers in 2016,[10] provide a highly promising purely organic strategy to overcome this challenge. The core principle of MR-TADF materials relies on the incorporation of alternating electron-donating and -withdrawing atoms (*e.g.*, B and N) within a rigid and planar π-conjugated skeleton. This atomic arrangement induces alternating localization of the frontier molecular orbitals (FMOs) on specific atomic sites, which not only results in a small singlet-triplet energy gap (ΔE_{ST}) that enables efficient reverse intersystem crossing (RISC) but also imparts the non-bonding orbital character to the FMOs, thereby minimizing structural relaxation and vibronic coupling and yielding exceptionally sharp emission profiles. Thereby, MR-TADF materials inherently exhibit an ultra-narrow FWHM (<40 nm), making them particularly well-suited for fabricating high-efficiency deep-blue OLEDs that satisfy the stringent requirements of the BT.2020 standard.[11–13]

However, the inherent rigid and extended planar structures of MR-TADF materials also present a significant dilemma. In the solid state, this molecular architecture renders them highly prone to strong intermolecular π–π stacking, which induces severe aggregation-caused quenching (ACQ), along with spectral broadening and red-shifting.[14] This necessitates the use of MR-TADF materials at extremely low doping concentrations (typically <3 wt%), which significantly increases the cost of device fabrication processes and limits their application in simplified device structures.[15–19] To mitigate these issues, conventional approaches involve introducing bulky substituents (*e.g.*, carbazole, triphenylamine, fluorene, *etc.*) onto the periphery of MR-TADF molecules to suppress intermolecular π–π stacking *via* steric hindrance, thereby inhibiting ACQ effects.[20–26] However, this approach entails significant drawbacks: (1) the incorporation of multiple bulky substituents substantially increases synthetic complexity and cost; (2) many such substituents are not electronically inert and inevitably perturb FMOs of the core or extend π-conjugation, leading to undesirable red-shifts in emission that hinder the compliance with the BT.2020 blue standard.

In contrast, recent studies have shifted toward decorating the MR-TADF periphery with small, electronically inert steric groups. For instance, Yang *et al.* reported mesityl-functionalized **DOBN** emitters that exhibited concentration-independent deep-blue emission with external quantum efficiencies (EQEs) exceeding 30%, owing to the effective suppression of ACQ by steric groups.[27] Hattori and co-workers developed narrowband near-UV and deep-blue MR-TADF materials *via* a tri-*ortho*-lithiation-borylation strategy, where steric effects enabled efficient EL performance at the 5 wt% doping level.[28] Our group recently demonstrated that simple methyl modification suppresses ACQ while simultaneously enhancing rates of RISC (k_{RISC}) and photoluminescence quantum yield (PLQY), yielding a state-of-the-art deep-blue MR-TADF emitter (**BN-M3**) with an EQE_{max} of 34.8% and minimal efficiency roll-off.[29] Collectively, these findings suggest that the strategic incorporation of small substituents at optimal positions can effectively suppress ACQ and minimize perturbations to the FMOs. This strategy preserves synthetic simplicity while retaining the high-

efficiency deep-blue emission required to meet the stringent BT.2020 standard. Nevertheless, research in this area remains in its infancy, and the underlying mechanisms governing how the number and position of substituents synergistically influence the photophysical properties and device performance of deep-blue MR-TADF emitters are still inadequately understood. This persistent knowledge gap continues to impede the broader adoption of this promising strategy for the rational design of next-generation BT.2020-compliant OLED materials.

Herein, we present a systematic structure–property investigation of deep-blue MR-TADF emitters to elucidate the role of methyl substitution regiochemistry and multiplicity in excited-state dynamics and device performance. Using **DABNA-NP** as a model MR-TADF scaffold, four methylated derivatives (**1M-BN**, **2M-BN**, **3M-BN**, and **4M-BN**) were rationally designed to modulate steric hindrance and intermolecular packing without compromising color purity (Fig. 1). The introduction of small methyl groups effectively disrupts intermolecular π–π stacking, endowing all derivatives with excellent resistance to ACQ while maintaining deep-blue emission. Crucially, we identify di-*ortho* substitution as the key structural requirement for achieving maximum molecular rigidity. Theoretical analyses demonstrate that di-*ortho*-methyl substitution on the peripheral phenyl rings (**2M-BN**, **3M-BN**, and **4M-BN**) more effectively restricts intramolecular vibrational and rotational modes than mono-*ortho* substitution (**1M-BN**). This geometric constraint significantly suppresses structural relaxation in the excited state, as quantitatively evidenced by reduced Huang–Rhys factors and smaller root-mean-square displacement (RMSD) values. Consequently, **2M-BN**, **3M-BN**, and **4M-BN** exhibit higher PLQY and narrower FWHM compared to **1M-BN**. Further methylation exerts only minimal influence on the luminescent properties, highlighting di-*ortho*-methylation as the optimal "ring-locking" motif for maximizing luminescent performance. Additionally, OLEDs incorporating these emitters delivered concentration-independent, high-efficiency deep-blue EL that satisfies the BT.2020 standard. Notably, OLEDs based on **2M-BN** exhibited an EQE_{max} of 23.3–26.9% across a broad doping range of 1–15 wt%, accompanied by stable CIE_y coordinates of 0.040–0.046. These results establish a direct mechanistic link among steric methylation, excited-state rigidity, and device performance, demonstrating that precise regioselective locking with small substituents can outperform conventional bulky-substituent strategies by simultaneously preserving color purity and enhancing device efficiency. This work offers a general molecular design principle for high-color-purity MR-TADF emitters.

Results and discussion

Synthesis and single-crystal analysis

All four compounds were synthesized *via* a concise two-step procedure, and their structures were fully confirmed by ^{1}H and ^{13}C nuclear magnetic resonance (NMR) spectroscopy, high-resolution mass spectrometry (HRMS) and elemental analyses (EA) (Fig. S1–S21). Based on the cyclic voltammetry measurements and ultraviolet-visible (UV-vis) absorption spectra, the highest occupied molecular orbital (HOMO) energy levels of **1M-BN**, **2M-BN**, **3M-BN** and **4M-BN** were determined to be −5.24, −5.27, −5.25 and −5.23 eV, respectively, while the lowest unoccupied molecular orbital (LUMO) energy levels were calculated to be −2.54, −2.53, −2.53 and −2.52 eV for these four compounds. Thermal properties were evaluated by differential scanning calorimetry (DSC) and thermogravimetric analysis (TGA). All four compounds exhibit excellent thermal stability, with 5% weight loss temperatures (T_d, 5%) ranging from 327.5 to 374.6 °C. No glass transition temperatures (T_g) were observed from room temperature to 240 °C (Fig. S22 and Table S1). These favorable thermal characteristics render them well suited for OLED device fabrication. The molecular structures, synthetic routes, and single-crystal structures of the four target molecules are depicted in Fig. 2. Single crystals suitable for X-ray diffraction were obtained by slow solvent evaporation. Crystallographic analysis reveals that the methyl substitution on the peripheral phenyl rings induces pronounced molecular distortion relative to the planar MR core, leading to large torsion angles in the range of 70.7°–87.3°. As depicted, the intermolecular face-to-face distance of **1M-BN** is measured to have a moderate value of 3.575 Å. Such close packing tends to facilitate unfavorable intermolecular electronic coupling, thereby leading to ACQ along with the broadening and redshifting of the emission spectra. In contrast, with the incorporation of di-*ortho*-methyl at the peripheral phenyl rings (**2M-BN**, **3M-BN**, and **4M-BN**), the intermolecular distances sharply increase to 5.864–6.092 Å. Such expanded intermolecular separations effectively suppress detrimental π–π stacking, which is essential for achieving concentration-independent MR-TADF emitters. Notably, the comparatively shorter intermolecular distance observed for **1M-BN** suggests a reduced ability to mitigate ACQ relative to the other methylated analogues.

Photophysical properties

The photophysical properties of the four compounds were investigated in dilute toluene solution ($\approx 10^{-5}$ M). As shown in Fig. 3a, all emitters show distinct absorption bands at 421 nm (**1M-BN**), 429 nm (**2M-BN**), 430 nm (**3M-BN**), and 432 nm (**4M-BN**), which are assigned to short-range charge transfer (SRCT) transitions characteristic of MR-type chromophores. Correspondingly, sharp fluorescence emission peaks are observed at 442 nm (FWHM = 30 nm) for **1M-BN**, 442 nm (FWHM = 22 nm) for **2M-BN**, 445 nm (FWHM = 21 nm) for **3M-BN**, and 446 nm (FWHM = 21 nm) for **4M-BN**, resulting in Stokes shifts of 21, 13, 15, and 14 nm, respectively. Notably, all four emitters exhibit deep-blue emission, confirming that methyl substitution induces negligible bathochromic shifts while effectively preserving high color purity. The PLQYs increase progressively from 77% for **1M-BN** to 88%, 88%, and 93% for **2M-BN**, **3M-BN**, and **4M-BN**, respectively. Among them, **1M-BN** displays a noticeably broader emission bandwidth, a larger Stokes shift, and a substantially lower PLQY than the other derivatives. These observations suggest a comparatively less rigid molecular framework for **1M-BN**, which likely permits enhanced intramolecular vibrational and rotational relaxation in the excited state, thereby facilitating non-radiative pathways.

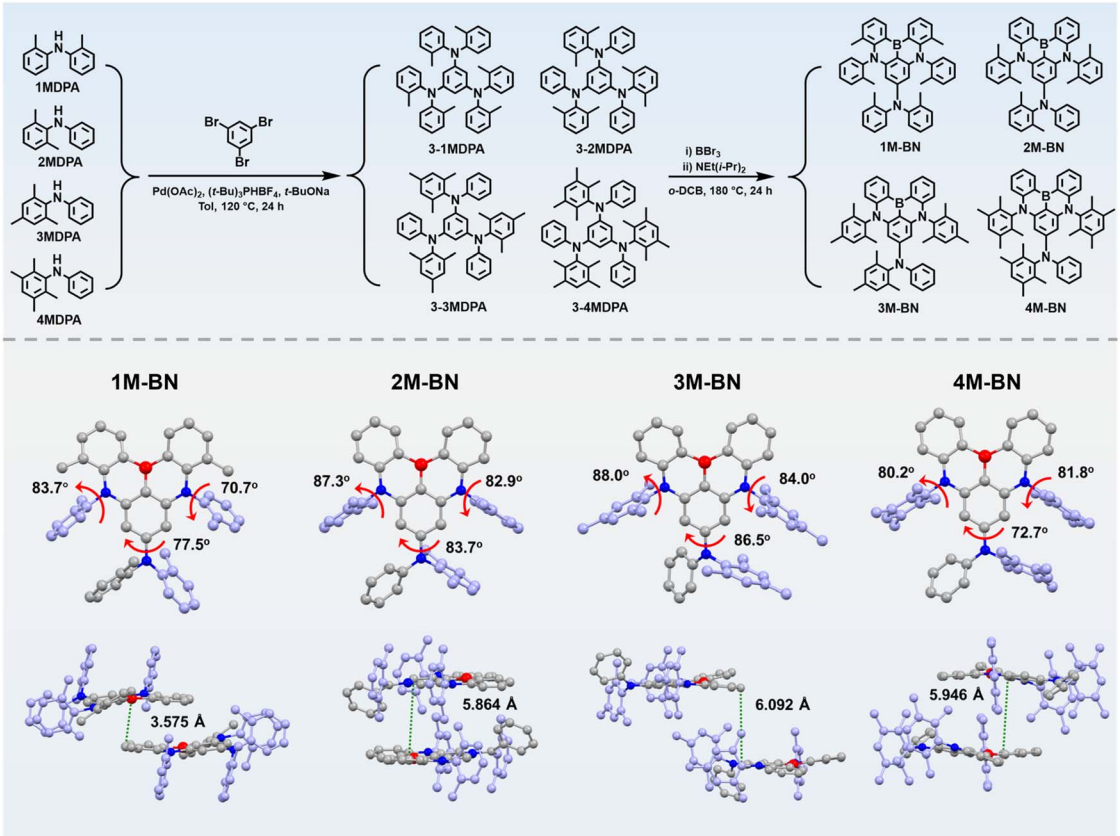

Fig. 2 The synthesis routes and single-crystal structures of the four emitters.

Phosphorescence spectra recorded at 77 K reveal small ΔE_{ST} values of 0.14–0.15 eV for all four compounds, which are conducive to an efficient RISC process and high exciton utilization. In addition, all four emitters show a positive solvatochromic behavior in their photoluminescence (PL) spectra, manifested by slight bathochromic shifts and marginally broadened FWHMs with increasing solvent polarity, consistent with the SRCT transition nature (Fig. S23). These results reveal that differences in methyl substitution predominantly influence the nonradiative decay processes through modulation of molecular rigidity, thereby governing the luminescent properties of the emitters.

Next, the photophysical properties of these four emitters were investigated in vacuum-deposited 1 wt% doped 3,3-bis(*N*-carbazolyl)-1,1′-biphenyl (mCBP) films. The corresponding photophysical data are shown in Fig. 3b and summarized in Table 1. The emission maxima/FWHM values of the **1M-BN**, **2M-BN**, **3M-BN**, and **4M-BN** films are 444/36 nm, 446/25 nm, 447/24 nm, and 451/23 nm, respectively. Relative to their spectra in dilute solution, the doped films exhibit slight red-shifts and modest spectral broadening, as expected from weak intermolecular π–π interactions in the aggregated state. Moreover, the FWHM of **1M-BN** increases most markedly (by 6 nm) in the film, whereas those for **2M-BN**, **3M-BN**, and **4M-BN** broaden by only 2–3 nm. This pronounced difference underscores the inferior resistance of **1M-BN** to ACQ relative to the other three derivatives, which is further corroborated by its shorter intermolecular π–π distance observed in the single-crystal structures. Furthermore, these doped films maintained exceptionally high PLQYs of 92% (**1M-BN**), 95% (**2M-BN**), 99% (**3M-BN**), and 98% (**4M-BN**). Consistent with its solution-state behavior, **1M-BN** displays the largest FHWM and the lowest PLQY among the series, indicative of its relatively lower molecular rigidity. To gain deeper insights into the excited-state dynamics, transient photoluminescence (TRPL) decay characteristics were assessed (Fig. 3c). All four doped films exhibited biexponential kinetics, with distinct prompt (τ_p) and delayed (τ_d) components typical of TADF behavior. The determined lifetimes (τ_p/τ_d) were 6.42 ns/16.7 μs for **1M-BN**, 5.28 ns/12.6 μs for **2M-BN**, 6.45 ns/18.9 μs for **3M-BN**, and 4.98 ns/15.1 μs for **4M-BN**. Oxygen-dependent PL spectra confirm the participation of triplet excitons in all four compounds, as indicated by the enhanced emission under vacuum conditions (Fig. S24). Temperature-dependent TRPL decay measurements further confirm the TADF nature of these emitters, as evidenced by the pronounced enhancement of the delayed component with increasing temperature (Fig. S25). Based on these photophysical data, key rate constants were calculated and are also listed in Table 1. The rate constants for non-radiative decay (k_{nr}) and k_{RISC} are found to be 3.5×10^6 s^{-1} and 2.2×10^5 s^{-1} for **1M-BN**, 3.2×10^6 s^{-1} and 2.2×10^5 s^{-1} for **2M-BN**, 0.63×10^6 s^{-1} and 1.3×10^5 s^{-1} for **3M-BN**, and 2.2×10^6 s^{-1} and 1.2×10^5 s^{-1} for **4M-BN**, respectively. These results clearly demonstrate that increased methyl substitution effectively suppresses non-

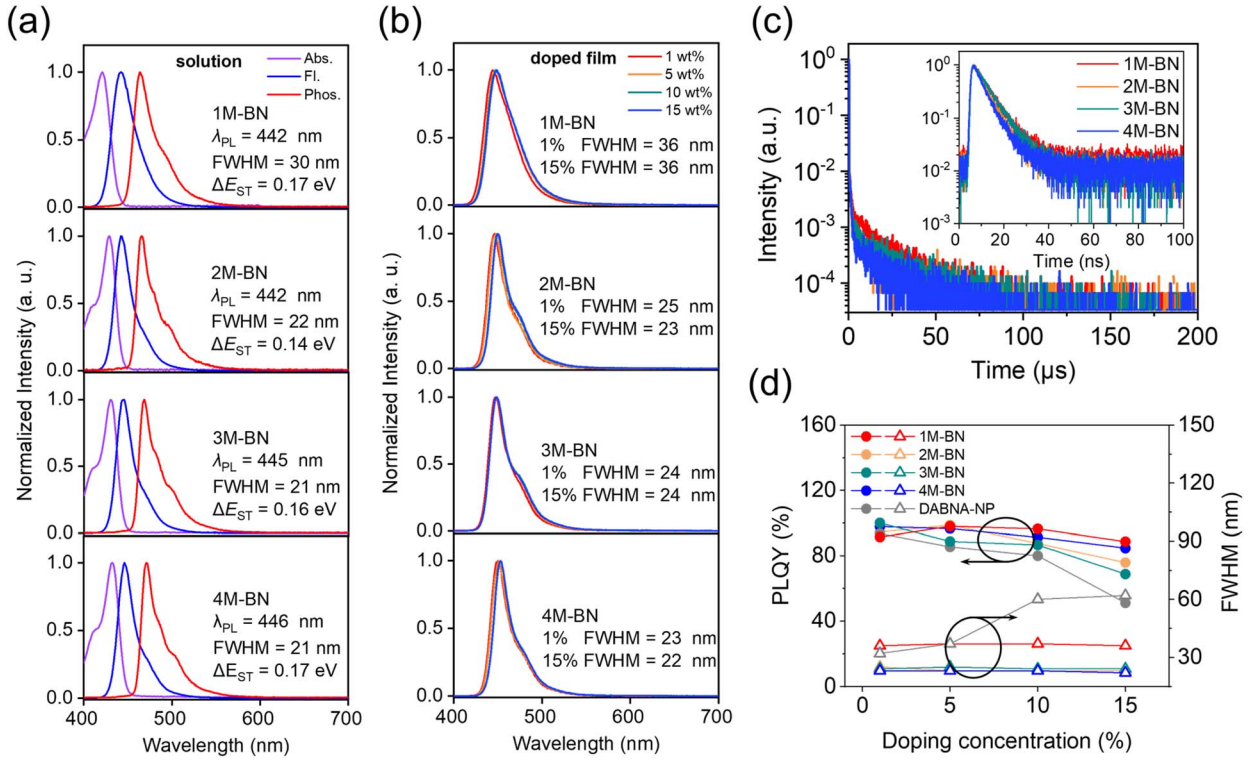

Fig. 3 (a) UV-vis absorption and fluorescence/phosphorescence spectra of **1M-BN**, **2M-BN**, **3M-BN** and **4M-BN** in toluene (10^{-5} M). (b) Steady-state PL spectra measured at 300 K for the doped films of **1M-BN**, **2M-BN**, **3M-BN**, and **4M-BN** (1 wt%, 5 wt%, 10 wt% and 15 wt% in mCBP). (c) Transient decay curves of emitters (1 wt% in mCBP) in the doped film. (d) PLQYs and FWHMs of emitters in the doping concentration range of 1–15 wt%.

radiative decay while maintaining efficient RISC, thereby underpinning the superior solid-state emission performance of the more highly methylated derivatives. To systematically evaluate the concentration-independent emission behavior in the solid state, the conventional MR-TADF emitter **DABNA-NP** was synthesized as a reference.[30] Doped mCBP films with concentrations of 1, 5, 10, and 15 wt% were prepared for comparative photophysical studies. The corresponding data of **DABNA-NP** are presented in Fig. S26 and Table S2. As depicted in Fig. 3b, d and S26, all four molecules in this research exhibit remarkable resistance to the quenching caused by concentration, in sharp contrast to **DABNA-NP**. With increasing doping levels, the emission maxima and FWHMs remain essentially unchanged, while relatively high PLQYs are well preserved. This outstanding concentration tolerance is attributed to the intramolecular steric hindrance by the methyl substituents, which effectively disrupts unfavorable intermolecular π–π stacking and thereby mitigates the inherent ACQ effect typical of planar MR-TADF emitters.[31] Such robustness against ACQ effects is particularly advantageous for the fabrication of high-performance MR-TADF OLEDs at high doping levels, enabling simplified device architectures, improved reproducibility, and enhanced manufacturability.

Table 1 Summary of photophysical properties

Emitter	λ_{abs} [a] [nm]	λ_{em} [b] [nm]	FWHM [c] [nm]	ΔE_{ST} [d] [eV]	τ_p [e] [ns]	τ_d [f] [μs]	k_r [g] [10^7 s^{-1}]	k_{nr} [h] [10^6 s^{-1}]	k_{ISC} [i] [10^8 s^{-1}]	k_{RISC} [j] [10^5 s^{-1}]	PLQY [k] [%]
1M-BN	421	442	30	0.14	6.42	16.3	4.0	3.5	1.1	2.2	77/92
2M-BN	429	442	22	0.14	5.28	13.9	6.0	3.2	1.3	2.2	88/95
3M-BN	430	445	21	0.14	6.45	18.7	6.2	0.63	0.92	1.3	88/99
4M-BN	432	446	21	0.15	4.98	15.3	10.5	2.2	0.93	1.2	93/98

[a] Maximum wavelength of UV-vis absorption recorded in toluene solutions (10^{-5} M). [b] PL emission peak recorded in toluene solutions (10^{-5} M). [c] FWHM recorded in toluene (10^{-5} M). [d] S_1–T_1 energy gap (ΔE_{ST}) measured in toluene solution (10^{-5} M). [e] Prompt lifetime (τ_p). [f] Delayed lifetime (τ_d). [g] Rate constants of radiative decay (k_r). [h] Non-radiative decay (k_{nr}). [i] Intersystem crossing (k_{ISC}). [j] Reverse intersystem crossing (k_{RISC}). [k] Absolute photoluminescence quantum yield (PLQY), measured from toluene solutions (10^{-5} M)/1 wt% doped films in mCBP.

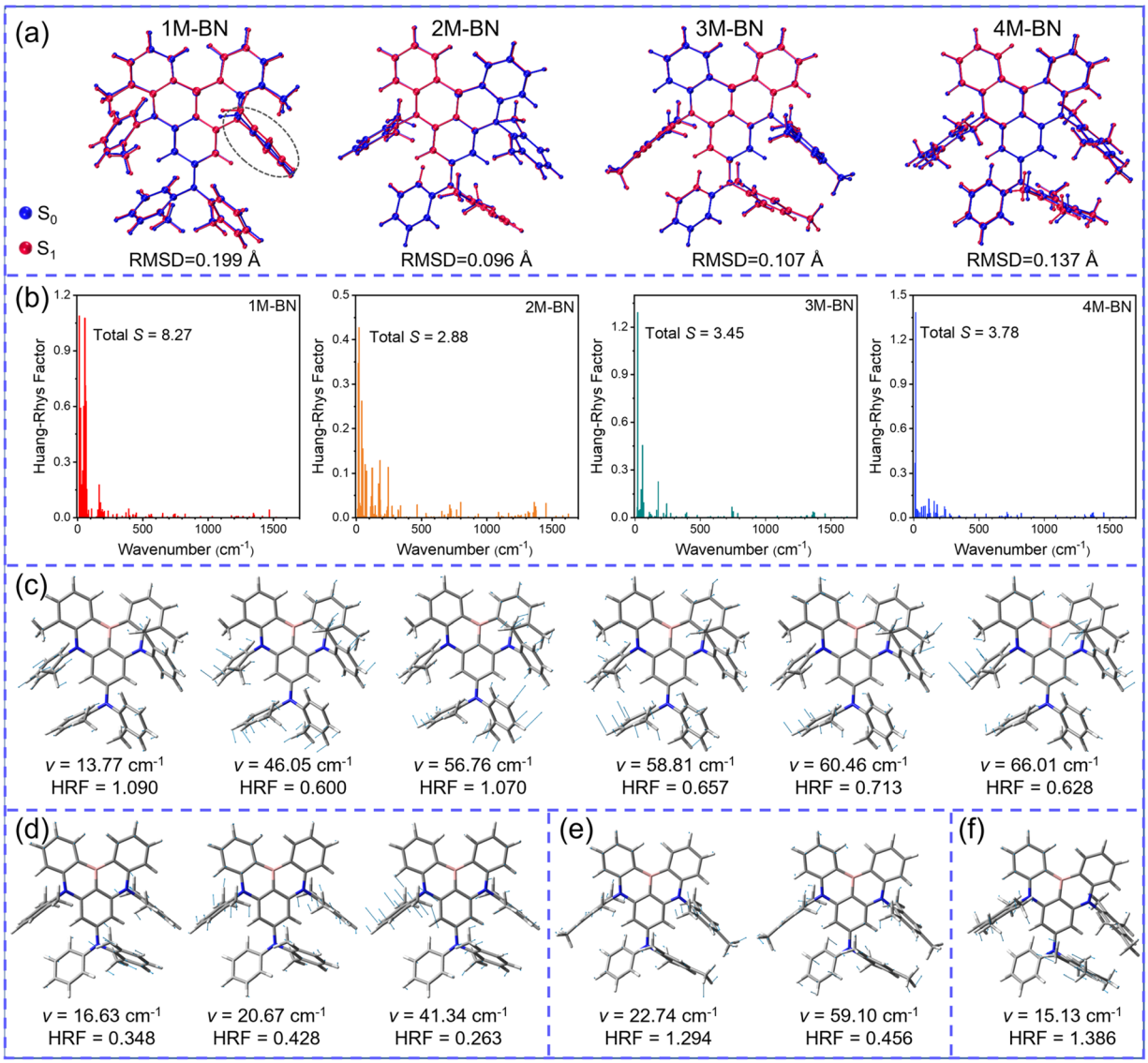

Fig. 4 (a) RMSD comparison between S_0 (blue) and S_1 (red) states. (b) HRFs *versus* frequencies for the $S_1 \rightarrow S_0$ transition of the four emitters. The representative vibration modes for the $S_1 \rightarrow S_0$ transition of (c) **1M-BN**, (d) **2M-BN**, (e) **3M-BN** and (f) **4M-BN**.

Theoretical calculations

To provide a more systematic understanding for the distinct properties observed among the four compounds, density functional theory (DFT) and time-dependent DFT (TD-DFT) calculations were performed at the B3LYP-D3(BJ)/6-31G(d,p) level. For all four emitters, the FMOs are predominantly localized on individual atoms (Fig. S27), giving rise to the spatially separated HOMO/LUMO distributions, a hallmark feature of MR-TADF systems. Intriguingly, the incorporation of methyl groups exerts a minimal perturbation on the FMOs. Increasing the number of methyl groups induces merely marginal bathochromic shifts in the calculated energy gaps, confirming that the intrinsic deep-blue emission of the MR core is well preserved. Furthermore, theoretical calculations reveal that **2M-BN**, **3M-BN**, and **4M-BN** possess significantly larger oscillator strengths (*f*) compared to **1M-BN**, consistent with their experimentally observed higher PLQYs. Analysis of the natural transition orbitals (NTOs) shows that the $S_0 \rightarrow S_1$ and $S_0 \rightarrow T_1$ transitions in all four molecules are dominated by HOMO-to-LUMO transitions with nearly identical spatial distributions (Fig. S28), which result in relatively small SOC matrix elements $\langle S_1|\hat{H}_{SOC}|T_1\rangle$.[32] In contrast, the NTOs of the higher-lying triplet state (T_2) differ substantially from those of S_1, lead to enhanced SOC between S_1 and T_2. The calculated $\langle S_1|\hat{H}_{SOC}|T_2\rangle$ values are 0.586 cm^{-1}, 0.349 cm^{-1}, 0.341 cm^{-1}, and 0.283 cm^{-1} for **1M-BN**, **2M-BN**, **3M-BN**, and **4M-BN**, respectively. Consequently, the combination of small ΔE_{ST} and appreciable SOC is expected to promote efficient RISC according to Fermi's golden rule, thereby accounting for the high k_{RISC} values observed experimentally.

To further elucidate the influence of methyl substitution on intramolecular motions, the RMSD between the S_0 and S_1

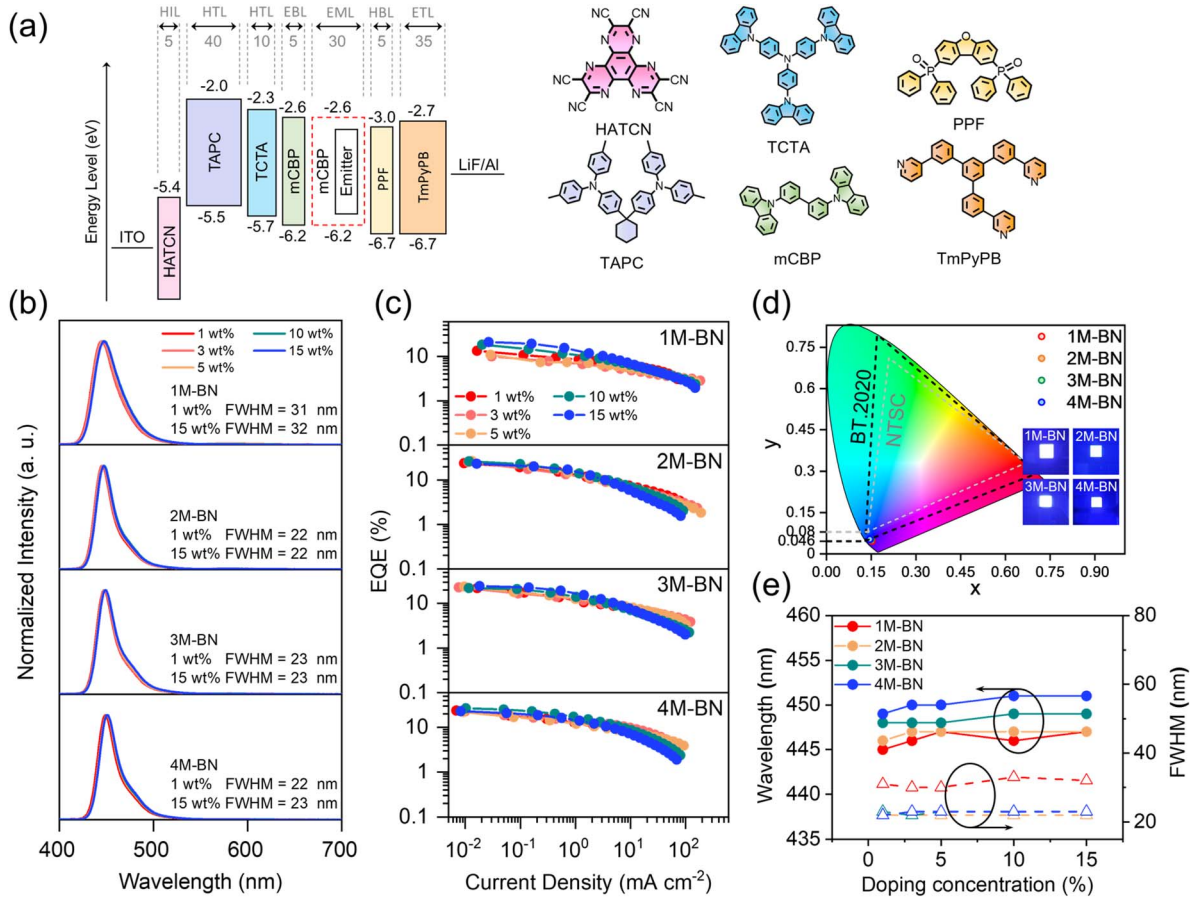

Fig. 5 (a) The OLED architectures and the molecular structure of the above functional materials. (b) EL spectra (recorded at 100 cd m^{-2}) of **1M-BN**, **2M-BN**, **3M-BN** and **4M-BN** based OLEDs at different doping concentrations. (c) EQE-current density curves of **1M-BN**, **2M-BN**, **3M-BN** and **4M-BN** based OLEDs at different doping concentrations. (d) Commission Internationale de l' Éclairage (CIE) (*x*, *y*) coordinates of **1M-BN**, **2M-BN**, **3M-BN** and **4M-BN** based OLEDs at 1 wt% doping concentrations. (Grey dashed line: National Television Standards Committee (NTSC) color gamut; black dashed line: BT.2020 color gamut). (e) EL wavelengths and FWHMs of emitters at 1, 3, 5, 10, and 15 wt% doping concentration.

geometries and the $S_1 \rightarrow S_0$ reorganization energy (Λ_{reorg}) were simulated to investigate the structural relaxation (Fig. 4a and S29). **2M-BN**, **3M-BN**, and **4M-BN** exhibit significant structure rigidity, characterized by small RMSD and Λ_{reorg} values of 0.096 Å/734 cm^{-1}, 0.107 Å/747 cm^{-1}, and 0.137 Å/770 cm^{-1}, respectively, indicating minimal geometric distortion under excitation. However, **1M-BN** shows notable differences between the S_0 and S_1 geometries (highlighted by the gray circle in Fig. 4a), accompanied by significantly larger RMSD and Λ_{reorg} values (0.199 Å/921 cm^{-1}). This comparison clearly indicates that di-*ortho*-methyl substitution effectively suppresses benzene-ring motion and enhances overall molecular rigidity. Additionally, the Huang–Rhys factors (HRFs) and representative vibration modes associated with the $S_1 \rightarrow S_0$ transition were analyzed (Fig. 4b). All four compounds displayed similar types of vibrational modes (Fig. 4c–f), with the HRFs being small and primarily contributed by twisting vibrations at low frequencies (*e.g.*, 1.090 at 13.77 cm^{-1}, 0.600 at 46.05 cm^{-1}, 1.070 at 56.76 cm^{-1}, 0.657 at 58.81 cm^{-1}, 0.713 at 60.46 cm^{-1} and 0.628 at 66.01 cm^{-1} for **1M-BN**; 0.348 at 16.63 cm^{-1}, 0.428 at 20.67 cm^{-1} and 0.263 at 41.34 cm^{-1} for **2M-BN**; 1.294 at 22.74 cm^{-1} and 0.456 at 59.10 cm^{-1} for **3M-BN**; 1.386 at 15.13 cm^{-1} for **4M-BN**), whereas contributions from high-frequency modes remain negligible. Strikingly, **1M-BN** shows markedly stronger HRFs for low-frequency twisting vibrations compared to the more heavily methylated derivatives, indicating more pronounced vibrational coupling between the S_1 and S_0 states. Collectively, these results demonstrate that di-*ortho*-methyl substitution acts as an effective "ring-locking" strategy that can effectively restrict rotational and twisting motions of the peripheral phenyl rings, thereby reducing excited-state structural relaxation and suppressing nonradiative decay pathways. This vibrational confinement provides a clear mechanistic explanation for the superior color purity (narrower FWHM) and higher luminescence efficiency (enhanced PLQY) observed in the more heavily methylated MR-TADF emitters.

Electroluminescence

To investigate their EL properties, vacuum-evaporated devices employing the four emitters as deep-blue dopants were fabricated. The device architecture and EL performance including EL spectra, current density, luminescence, EQE *vs.* current

Table 2 Summary of the EL data

Emitter	X^a [wt%]	$V_{on}{}^b$ [V]	$\lambda_{EL}{}^c$ [nm]	FWHM^d [nm]	$CE_{max}{}^e$ [cd A^{-1}]	$PE_{max}{}^f$ [lm W^{-1}]	$EQE_{max/1000}{}^g$ [%]	CIE^h [x, y]
1M-BN	1	4.4	445	31	6.0	4.3	13.3/3.89	0.155, 0.045
	3	4.3	446	30	5.2	3.8	10.0/3.50	0.157, 0.049
	5	4.4	447	30	5.2	3.7	10.8/3.73	0.154, 0.051
	10	4	447	33	8.6	6.8	18.3/3.99	0.150, 0.050
	15	3.9	447	32	10.0	8.0	21.0/3.88	0.148, 0.047
2M-BN	1	4.1	446	22	9.6	7.3	24.0/4.42	0.154, 0.040
	3	4	447	22	10.9	8.5	25.4/3.80	0.153, 0.045
	5	3.9	447	22	11.5	9.2	26.9/3.46	0.152, 0.045
	10	3.9	447	22	11.3	9.1	26.5/2.85	0.153, 0.045
	15	3.7	447	22	10.1	8.6	23.3/-	0.154, 0.046
3M-BN	1	4.3	448	23	10.0	7.2	22.1/5.77	0.153, 0.046
	3	4.2	448	22	10.9	8.3	22.9/5.92	0.152, 0.049
	5	4.1	448	23	11.7	9.0	24.0/6.08	0.151, 0.051
	10	3.7	449	23	11.0	9.3	22.1/3.85	0.149, 0.051
	15	3.5	449	23	12.5	11.2	24.5/3.45	0.147, 0.051
4M-BN	1	4.4	449	22	11.2	8.2	23.9/5.37	0.150, 0.048
	3	4.5	450	23	11.3	7.9	22.8/7.16	0.147, 0.051
	5	4.1	450	23	11.2	8.5	22.0/5.94	0.149, 0.053
	10	3.9	451	23	13.7	10.9	26.7/4.51	0.146, 0.052
	15	3.6	451	23	12.0	10.5	23.1/—	0.145, 0.052

[a] Doping concentration. [b] Voltage measured at 1 cd m^{-2}. [c] EL peak wavelength. [d] Full-width at half-maximum. [e] Maximum current efficiency. [f] Maximum power efficiency. [g] Maximum external quantum efficiency/external quantum efficiency at 1000 cd m^{-2}. [h] Commission Internationale de l' Éclairage ($CIE_{x,y}$) coordinates. λ_{EL}, FWHM and CIE coordinates are reported at 1000 cd m^{-2}.

density, and current/power efficiencies (CE/PE) *vs.* current density are illustrated in Fig. 5, S30 and S31, and summarized in Table 2. The optimized muladverstilayer OLED architecture was as follows: indium tin oxide (ITO)/HATCN (1,4,5,8,9,11-hexaazatriphenylene-hexacarbonitrile, 5 nm)/TAPC (1,1-bis[(di-4-tolylamino)phenyl]cyclohexane, 40 nm)/TCTA (tris(4-carbazolyl-9-ylphenyl)amine, 10 nm)/mCBP (3,3-bis(*N*-carbazolyl)-1,1′-biphenyl, 5 nm)/mCBP: emitter (30 nm)/PPF (2,8-bis(diphenylphosphoryl)dibenzo[*b*,*d*]furan, 6 nm)/TmPyPB (1,3,5-tris(*N*-phenylbenzimidazol-2-yl)benzene, 40 nm)/LiF (1 nm)/Al (130 nm). In this architecture, HATCN and LiF functioned as the hole- and electron-injection layers, respectively, TAPC, TCTA, and TPBi acted as charge-transport layers, PPF served as the hole-blocking layer, and mCBP simultaneously functioned as the electron-blocking layer and the host matrix.

At a doping concentration of 1 wt%, pronounced differences in EL performance were observed among the four emitters (Fig. 5b and c). The device based on **1M-BN** exhibited deep-blue EL with a relatively narrower bandwidth (FWHM = 31 nm) and a modest EQE_{max} of 13.3%. In sharp contrast, devices incorporating **2M-BN**, **3M-BN**, and **4M-BN** exhibit significantly narrower EL spectra (FWHM = 22–23 nm) together with markedly enhanced EQE_{max} values exceeding 22%. Notably, **2M-BN** and **3M-BN** devices achieve efficient deep-blue emission that satisfies the BT.2020 standard, delivering EQE_{max} values of 24.0% and 22.1% with CIE coordinates of (0.154, 0.040) and (0.153, 0.046), respectively. The inferior EL performance of **1M-BN** closely reflects its PL characteristics, including a broader emission profile and lower PLQY in both solution and doped films, whereas the superior EL efficiency and spectral purity of **2M-BN**, **3M-BN**, and **4M-BN** arise from enhanced molecular rigidity and suppressed nonradiative decay pathways. In addition, the EL spectra exhibit excellent stability (Fig. S32), with negligible changes upon increasing the operating voltage from ~4 to ~8.5 V, indicating balanced charge injection and efficient exciton recombination.

To further examine concentration-independent EL behavior, OLEDs with higher doping concentrations of 3, 5, 10, and 15 wt% were fabricated. As shown in Fig. 5b and e, devices based on all four emitters maintained highly stable EL spectra upon increasing dopant concentration, with variations in the EL peak position and FWHM limited to within 2 nm. Meanwhile, device performance improves further at elevated doping levels, which can be attributed to the complete energy transfer from the host matrix to the emitter. The highest EQE_{max} values of 21.0% (at 15 wt%) for **1M-BN**, 26.9% (at 5 wt%) for **2M-BN**, 24.5% (at 15 wt%) for **3M-BN**, and 26.7% (at 10 wt%) for **4M-BN**, demonstrate their resistance to concentration quenching. Notably, similar to many deep-blue MR-TADF emitters, the devices exhibit a certain degree of efficiency roll-off at high luminance, with the EQEs remaining below 8% at 1000 cd m^{-2}. This efficiency roll-off is primarily attributed to the relatively low k_{RISC} values, which lead to insufficient triplet harvesting under high current density operation. Impressively, the devices based on **2M-BN** consistently satisfy the BT.2020 blue standard across the entire doping range, maintaining both superior EL efficiency and exceptional spectral stability. As summarized in Table S3, the OLED performance achieved here is highly competitive with the recently reported blue MR-TADF materials meeting CIE_y < 0.046. These results highlight di-*ortho*-methyl substitution as an effective ring-locking strategy to concurrently realize narrowband emission, high efficiency, and robust concentration tolerance, thereby providing a viable design principle for BT.2020-compliant deep-blue OLEDs.

Conclusions

In summary, we demonstrated a molecular design strategy that enables the simultaneous realization of high efficiency and strong resistance to ACQ in BT.2020-compliant deep-blue MR-TADF materials through minimalist methyl-based steric modulation. Systematic methyl substitution on the **DABNA-NP** scaffold effectively suppresses the intrinsic ACQ of the planar MR core while avoiding the spectral red-shifts commonly induced by bulky peripheral substituents. Combined photophysical and theoretical analyses reveal that di-*ortho*-methyl substitution induces a distinct "ring-locking" effect, which rigidifies the molecular framework and restricts vibrational/rotational modes. This vibrational confinement substantially suppresses non-radiative decay, leading to enhanced PLQYs and narrowed FWHMs while preserving high deep-blue color purity. Consequently, OLEDs based on the optimized emitter **2M-BN** achieved high EQE_{max}s of 23.3–26.9% with excellent concentration-independent performance over a broad doping range of 1–15 wt%, while strictly satisfying the BT.2020 blue standard (CIE_y = 0.040–0.046). These results establish a clear mechanistic relationship between precise regiochemistry and excited-state rigidity, demonstrating that optimization of the substitution pattern is as critical as the choice of substituent itself. This work establishes a clear and generalizable molecular engineering principle for developing high color-purity, quenching-resistant deep-blue MR-TADF materials for next-generation display technologies.

Author contributions

Li GY and Wang YY jointly participated in the synthesis of materials, single-crystal analysis, measurement of the photophysical properties, preparation and characterization of OLED devices and article writing and revision. Wu B helped in the theoretical calculation of the materials. Yang Z conceived the study and supervised the project. All authors contributed to the general discussion.

Conflicts of interest

There are no conflicts to declare.

Data availability

CCDC 2525523, 2525524, 2525526, and 2525527 contain the supplementary crystallographic data for this paper.[33a–c]

All data supporting the findings of this study are presented in the article and supplementary information (SI). Supplementary information is available. See DOI: https://doi.org/10.1039/d6sc02303g.

Acknowledgements

The authors gratefully acknowledge the financial support from the National Natural Science Foundation of China (NSFC: 52473195 and 52303250), Scientific Research Platforms and Projects of University of Department of Education of Guangdong Province (2024KCXTD009 and 2024ZDJS037), and Guangdong Special Support Program for Leading Talents (2024TX08C197). The authors gratefully acknowledge Dr Long Jiang from the Instrumental Analysis & Research Center of Sun Yat-Sen University for single-crystal X-ray diffraction measurements and structural analysis. The authors also wish to acknowledge HZWTECH for providing computation facilities. The authors also gratefully acknowledge the "Aggregate" software provided and authorized for use by the research team of Dr Bo Wu at Wuyi University.

References

1 I. S. Park, M. Yang, H. Shibata, N. Amanokura and T. Yasuda, *Adv. Mater.*, 2022, **34**, e2107951.
2 Y. M. Hu, M. Ng, X. Tang, C. Wang, Y. Huang, X. Zhu, P. Li, S. S. Chen and M.-C. Chen, *Adv. Mater.*, 2025, **37**, e10828.
3 G. Hong, X. Gan, C. Leonhardt, Z. Zhang, J. Seibert, J. M. Busch and S. Bräse, *Adv. Mater.*, 2021, **33**, e2005630.
4 R. M. Soneira, *J. Soc. Inf. Disp.*, 2016, **32**, 26–31.
5 M. Sugawara, S.-Y. Choi and D. Wood, *IEEE Signal Process. Mag.*, 2014, **31**, 170–174.
6 M. A. Baldo, D. F. O'Brien, Y. You, A. Shoustikov, S. Sibley, M. E. Thompson and S. R. Forrest, *Nature*, 1998, **395**, 151–154.
7 A. K. Pal, S. Krotkus, M. Fontani, C. F. R. Mackenzie, D. B. Cordes, A. M. Z. Slawin, I. D. W. Samuel and E. Zysman-Colman, *Adv. Mater.*, 2018, **30**, e1804231.
8 Y. H. Jung, D. I. Kim, S. Muruganantham, H. J. Cheon, S. C. Cha, H. Cho, E. Jeon, M. Y. Chae, Y.-H. Kim and J. H. Kwon, *Adv. Funct. Mater.*, 2025, **36**, e21312.
9 K. Xu, C. Zhang, L. Yang, F. Zhan, W. Lou, Y.-F. Yang, Y. She and G. Li, *Angew. Chem., Int. Ed.*, 2025, **64**, e202517695.
10 T. Hatakeyama, K. Shiren, K. Nakajima, S. Nomura, S. Nakatsuka, K. Kinoshita, J. Ni, Y. Ono and T. Ikuta, *Adv. Mater.*, 2016, **28**, 2777–2781.
11 H. Su, Y. Wang, K. Di, H. Yue, S. Huang, Y. Tian, Q. Zhang, H. Shao, R. Guo and L. Wang, *Adv. Funct. Mater.*, 2025, **35**, 2419679.
12 M. Xing, G. Chen, S. Wang, X. Yin, J. Liu, Z. Xue, N. Li, J. Miao, Z. Huang and C. Yang, *Adv. Funct. Mater.*, 2025, **35**, 2414635.
13 X. Cai, Y. Pan, C. Li, L. Li, Y. Pu, Y. Wu and Y. Wang, *Angew. Chem., Int. Ed.*, 2024, **63**, e202408522.
14 N. Peethani, N. Y. Kwon, C. W. Koh, S. H. Park, J. M. Ha, M. J. Cho, H. Y. Woo, S. Park and D. H. Choi, *Adv. Opt. Mater.*, 2024, **12**, 2301217.
15 S. Oda, W. Kumano, T. Hama, R. Kawasumi, K. Yoshiura and T. Hatakeyama, *Angew. Chem., Int. Ed.*, 2021, **60**, 2882–2886.
16 D. Li, S. Jiang, Q. Liu, R. Xu, G.-X. Yang, W. Li, S.-J. Su and X. Jiang, *Chem. Sci.*, 2026, **17**, 7056–7063.
17 E. Ravindran, H. E. Baek, H. W. Son, J. H. Park, Y.-H. Kim and M. C. Suh, *Adv. Funct. Mater.*, 2023, **33**, 2213461.
18 D. Wan, J. Zhou, Y. Yang, G. Meng, D. Zhang, L. Duan and J. Ding, *Adv. Mater.*, 2024, **36**, e2409706.

19 G. Chen, J. Wang, W. C. Chen, Y. Gong, N. Zhuang, H. Liang, L. Xing, Y. Liu, S. Ji, H.-L. Zhang, Z. Zhao, Y. Huo and B. Z. Tang, *Adv. Funct. Mater.*, 2023, **33**, 2211893.
20 J.-M. Jin, D. Liu, W.-C. Chen, C. Shi, G. Chen, X. Wang, L. Xing, W. Ying, S. Ji, Y. Huo and S.-J. Su, *Angew. Chem., Int. Ed.*, 2024, **63**, e202401120.
21 K. Xu, N. Li, Z. Ye, Y. Guo, Y. Wu, C. Gui, X. Yin, J. Miao, X. Cao and C. Yang, *Chem. Sci.*, 2024, **15**, 18076–18084.
22 P. Jiang, J. Miao, X. Cao, H. Xia, K. Pan, T. Hua, X. Lv, Z. Huang, Y. Zou and C. Yang, *Adv. Mater.*, 2022, **34**, e2106954.
23 C.-Z. Du, M. Mai, P.-H. Gao, Y.-C. Zhao, X.-Y. Gao, D. Zhang, L. Duan, C. Cui and X.-Y. Wang, *Chem. Sci.*, 2025, **17**, 5694–5700.
24 Y. Wang, Z. Ma, J. Pu, D. Guo, G. Li, Z. Chen, S.-J. Su, H. Deng, J. Zhao and Z. Chi, *Aggregate*, 2024, **5**, e585.
25 Z. Wang, Y. Song, D. Zhuang, T. Li, Y. Li and L. He, *Adv. Funct. Mater.*, 2026, e27474.
26 R. Ming, N. Li, Z. Chen, Z. Xue, J. Miao and Z. Huang, *Sci. China Mater.*, 2026, DOI: 10.1007/s40843-026-4094-8.
27 Z. Xue, Z. Xiao, Y. Zou, Z. Chen, J. Liu, Z. Huang and C. Yang, *Chem. Sci.*, 2025, **16**, 3655–3661.
28 Y. Kitamoto, A. Ogawa, M. Inakawa, Y. Fujimoto, M. Koshimizu, K. Oda, H. Taka, H. Kita and T. Hattori, *Angew. Chem., Int. Ed.*, 2025, **64**, e202510891.
29 Y. Wang, X. Guo, J. Bian, Z. Ma, X. Ge, L. Jiang, G. Li, Z. Chen, D. Guo, J. Zhao, Z. Yang, J. Miao and Z. Chi, *Adv. Mater.*, 2025, e14617.
30 Y. Wang, Y. Duan, R. Guo, S. Ye, K. Di, W. Zhang, S. Zhuang and L. Wang, *Org. Electron.*, 2021, **97**, 106275.
31 M. Liu, C. Li, L. Duan and D. Zhang, *Adv. Opt. Mater.*, 2026, **14**, e03140.
32 X. K. Chen, D. Kim and J. L. Bredas, *Acc. Chem. Res.*, 2018, **51**, 2215–2224.
33 (*a*) CCDC 2525523: Experimental Crystal Structure Determination, 2026, DOI: 10.5517/ccdc.csd.cc2qs0h1; (*b*) CCDC 2525524: Experimental Crystal Structure Determination, 2026, DOI: 10.5517/ccdc.csd.cc2qs0j2; (*c*) CCDC 2525526: Experimental Crystal Structure Determination, 2026, DOI: 10.5517/ccdc.csd.cc2qs0l4; (*d*) CCDC 2525527: Experimental Crystal Structure Determination, 2026, DOI: 10.5517/ccdc.csd.cc2qs0m5.